Electric and antiferromagnetic chiral textures at multiferroic domain walls

J.-Y. Chauleau, T. Chirac, S. Fusil, Vincent Garcia, W. Akhtar, J. Tranchida, P. Thibaudeau, I. Gross, C. Blouzon, A. Finco, et al.

Electric and antiferromagnetic chiral textures at multiferroic domain walls

J.-Y. Chauleau[1,2], T. Chirac[1], S. Fusil[3,8], V. Garcia[3], W. Akhtar[4], J. Tranchida[5§], P. Thibaudeau[5], I. Gross[4], C. Blouzon[1], A. Finco[4], M. Bibes[3], B. Dkhil[6], D.D. Khalyavin[7], P. Manuel[7], V. Jacques[4], N. Jaouen[2], M. Viret[1*]

[1]*SPEC, CEA, CNRS, Université Paris-Saclay, 91191 Gif-sur-Yvette, France.*
[2]*Synchrotron SOLEIL, 91192 Gif-sur-Yvette, France*
[3]*Unité Mixte de Physique, CNRS, Thales, Univ. Paris-Sud, Université Paris-Saclay, 91767 Palaiseau, France*
[4]*Laboratoire Charles Coulomb, Université de Montpellier and CNRS, 34095 Montpellier, France*
[5]*CEA – DAM le Ripault, BP 16, 37260 Monts, France*
[6]*Laboratoire Structures, Propriétés et Modélisation des Solides, CentraleSupélec, Université Paris Saclay, CNRS UMR8580, F-91190 Gif-Sur-Yvette, France*
[7]*ISIS Facility, STFC, Rutherford Appleton Laboratory, Didcot OX11 0QX, UK*
[8] *Université d'Evry, Université Paris-Saclay, Evry, France*

§ : now at 'Multiscale Science Department, Sandia National Laboratories, P.O. Box 5800, MS1322, 87185 Albuquerque, NM, United States'

* e-mail: michel.viret@cea.fr

Chirality, a foundational concept throughout science, may arise at ferromagnetic domain walls[1] and in related objects such as skyrmions[2]. However, chiral textures should also exist in other types of ferroics such as antiferromagnets for which theory predicts that they should move faster for lower power[3], and ferroelectrics where they should be extremely small and possess unusual topologies[4,5]. Here we report the concomitant observation of antiferromagnetic and electric chiral textures at domain walls in the room-temperature ferroelectric antiferromagnet $BiFeO_3$. Combining reciprocal and real-space characterization techniques, we reveal the presence of periodic chiral antiferromagnetic objects along the domain walls as well as a priori energetically unfavorable chiral ferroelectric domain walls. We discuss the mechanisms underlying their formation and their relevance for electrically controlled topological oxide electronics and spintronics.

Metallic ferromagnets have been the elemental bricks of spintronics for the last three decades and continue to hold promises on the basis of non-collinear chiral spin textures such as skyrmions. These topologically protected objects are envisioned to be the future of magnetic data storage thanks to their specific stability, dynamics, and scalability[2]. In parallel, antiferromagnets (AFs) are emerging as a new paradigm for spintronics[6]. They are intrinsically stable (being insensitive to spurious magnetic fields), scalable (no cross talk between neighbouring memory cells), and fast (switching frequencies in the THz regime). The opportunity of gathering the best of these two worlds and realize "antiferromagnetic skyrmions" is then tremendously appealing but faces at least two major challenges. The first one is to achieve antiferromagnetic chirality and the second one is to identify appropriate control stimuli to create, annihilate and move these chiral objects.

On one hand, chirality may naturally emerge at domain walls. The antiferromagnetic domain wall structure is a virtually uncharted territory but this is where translational symmetry is broken and spin rotation favoured. On the other hand, AF manipulation is hampered by the intrinsic lack of net magnetization, which prevents a straightforward magnetic actuation. This fundamental issue may be

addressed by different strategies. One of them relies on the generation of spin-transfer torque, mediated by spin currents, to act on the antiferromagnetic order. Antiferromagnetic switching was indeed recently demonstrated in specific non-centrosymmetric and conducting AFs such as CuMnAs[7]. However, the vast majority of AFs are insulating, which allows for low operation power and long spin wave propagation length, although spin-transfer torque remains to be explored in these compounds.

An alternative pathway could be to resort to materials known as multiferroics in which antiferromagnetism coexists with ferroelectricity. Some multiferroics also exhibit a magnetoelectric coupling between these orders, allowed in materials of certain symmetry classes introduced more than half a century ago[8,9]. In addition, multiferroic domain walls (DWs) may exhibit singular properties such as enhanced conductivity[10] associated with their ferroelectric (FE) order, in line with other exotic properties found in related ferroelastic or antiferroelectric materials[11,12]. The ability to write, erase and control domain walls in such systems is the cornerstone of *"the material is the machine"* concept[13]. Extending it to spintronics would offer opportunities unachievable with conventional magnetic materials.

In this study, we focus on bismuth ferrite[14] $BiFeO_3$ (BFO), the most prototypical multiferroic and one of the very few known materials presenting spin and dipole ordered phases well above room temperature. In addition to possessing a very large remanent electric polarization (100 $\mu C/cm^2$), BFO is a G-type antiferromagnet forced to rotate in a long-range (64 nm in the bulk) chiral cycloid because of the presence of magnetoelectric coupling between the two orders. The competition between symmetric and asymmetric exchange energies make the spins rotate in the plane defined by the electric polarization and the propagation vector, with an additional small periodic ferromagnetic canting of the moments in the transverse direction, in a spin density wave fashion (i.e. non-chiral). Interestingly, an AF skyrmion lattice is just the 'multi-*q*' version of the simple cycloid of bulk BFO, but this state is not stabilized in the bulk because no energy term plays a role equivalent to the magnetic field for ferromagnetic skyrmions. Our strategy here is to force a multi-*q* state using the frustration induced on the magnetic and ferroelectric orders by a high-density network of ferroelectric stripe domains. We use soft resonant elastic X-ray scattering (REXS), neutron scattering, piezoresponse force microscopy (PFM) and scanning nitrogen-vacancy (NV) magnetometry to observe periodic magnetic chiral objects stabilized at multiferroic domain walls showing ferroelectric chirality. These observations are also backed by spin dynamic simulations.

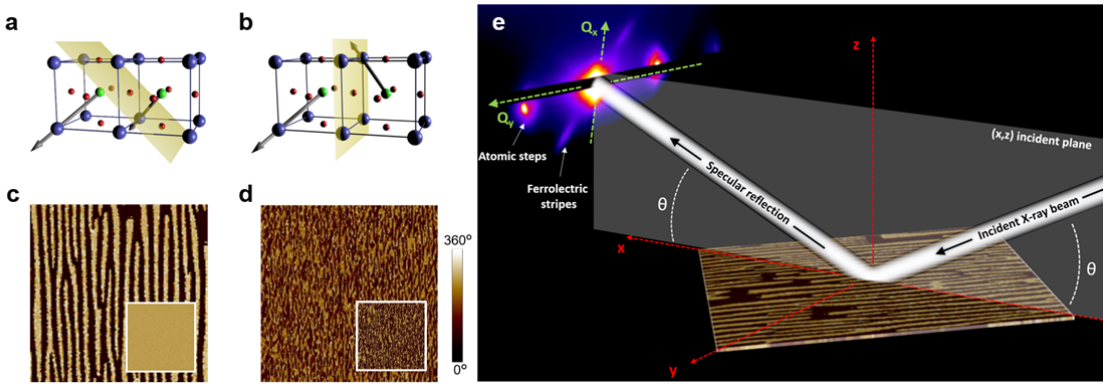

Figure 1: Self-organized ferroelectric patterns and principle of the resonant X-ray diffraction experiments. Schematics of **a**, the 71° domain wall in the $BiFeO_3$ / $SrRuO_3$ // $DyScO_3$ epitaxial heterostructure and **b**, the 109° domain wall in $BiFeO_3$ / $La_{0.7}Sr_{0.3}MnO_3$ // $DyScO_3$ formed by alternating ferroelectric polarization variants. The dark blue, red, and light green spheres stand for bismuth, oxygen, and iron ions, respectively and the light yellow planes represent the orientation of ferroelectric domain walls. The grey arrows represent electrical polarizations. **I**n-plane piezoresponse force microscopy images (4 × 4 μm^2) of **c**, the 71° and **d**, the 109° ferroelectric stripe patterns. Insets: corresponding out-of-plane PFM images. **e**, Sketch of the resonant elastic

X-ray scattering experiment in reflectivity geometry with Q_x and Q_y the directions in reciprocal space defined relative to the incident X-ray beam.

Two sets of BFO epitaxial layers have been grown by pulsed laser deposition on $DyScO_3$ substrates with buffer layers of either $SrRuO_3$ or $La_{0.7}Sr_{0.3}MnO_3$ (Methods). Because BFO has a rhombohedral symmetry (with a slight monoclinic distortion), 8 ferroelectric variants are possible along the {111} directions in the pseudo-cubic lattice. Mastering growth modes has allowed us to reduce the number of variants leading in some cases to highly ordered ferroelectric patterns. Our two representative samples are composed of ferroelectric stripes as characterized by (vectorial) PFM measurements (Fig. 1c,d). The first one has strong alternating contrast in the in-plane image and flat out-of-plane contrast (Fig. 1c) demonstrating that the stripes correspond to 71° FE domains (Fig. 1a) with a periodicity of about 210 nm. The stripes are less ordered in the second sample with dominant 109° FE domain walls (Fig. 1b) as shown in the two PFM images (Fig. 1d) with a 200 nm characteristic length scale.

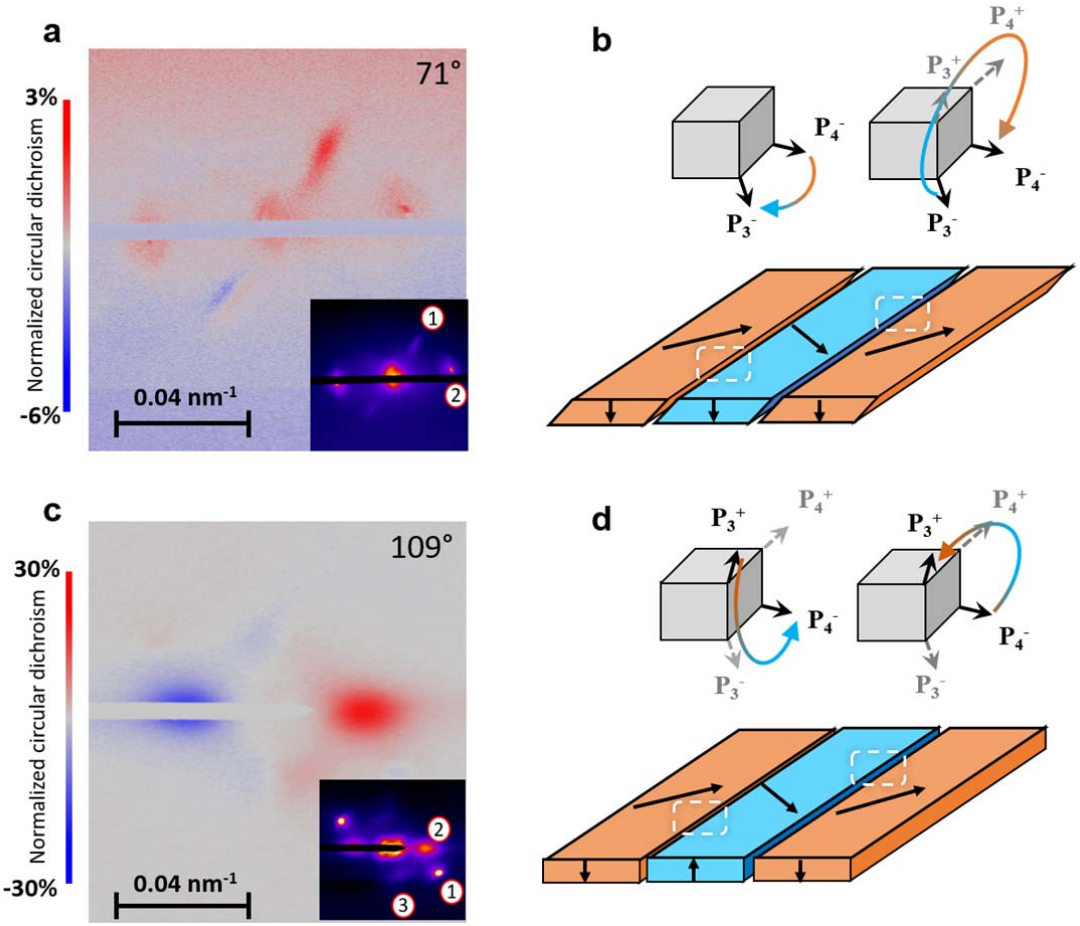

Figure 2: Chiral ferroelectric structures at domain walls. Dichroic patterns demonstrating that chirality is associated to electrical polarization in **a**, 71° and **c**, 109° domain walls. Insets: corresponding diffraction patterns around the O K edge (530 eV). In **a**, two pairs of diffraction spots result from the atomic steps of the substrate (2) and the periodic 71° FE structures (1). In **c**, three pairs of spots are caused by atomic steps (1) and 109° FE structures (2 & 3). Schematics of polarization (black arrows) leading to chiral arrangements for **b**, 71° and **d**, 109° domain walls.

REXS measurements were performed at the synchrotron Soleil on the SEXTANTS beamline in reflectivity geometry (Methods). In the soft energy range, the technique allows accessing complex charge, magnetic and orbital orders with nanometre spatial resolution. The diffracted intensity of a spatially modulated order in reciprocal space for a scattering vector Q is given by $I(Q) \propto |\sum_n f_n \cdot \exp(iQ \cdot r_n)|^2$ where f_n is the scattering amplitude of a single atom at position r_n. This scattering amplitude is a sum of several contributions, among which some resonant terms are substantially enhanced when the energy of incoming photons reaches absorption edges. They also strongly depend on polarization states of incoming and scattered photons. For electron dipole transitions and in the approximation of a cylindrical symmetry for the considered atoms, the resonant scattering amplitude f_n^{REXS} can be expanded in a sum of 3 main components[15–17]:

$$f_{\mathrm{n}}^{\mathrm{RES}} = f_0(\hat{\epsilon} \cdot \hat{\epsilon}') - i\, f_1(\hat{\epsilon} \times \hat{\epsilon}') \cdot m_{\mathrm{n}} + f_2(\hat{\epsilon}' \cdot m_{\mathrm{n}})(\hat{\epsilon} \cdot m_{\mathrm{n}})$$

where $\hat{\epsilon}$ and $\hat{\epsilon}'$ are the polarization states in the Jones formalism of the incident and diffracted beams, respectively, m_n, the local magnetization unit vector and f_0, f_1, f_2, the photon-energy-dependent resonance factors for, respectively, the monopole, magnetic dipole and quadrupole parts of the scattering amplitude. Interestingly, the second term of the right-hand-side, analogous to circular dichroism in absorption, is sensitive to m whereas the last term, analogous to linear dichroism in absorption, is sensitive to m^2 and therefore ideal to probe non-collinear antiferromagnetic orders. In lower symmetry lattices such as in ferroelectrics, parity-odd electric dipoles do not directly contribute in the electron-dipole approximation. However, the orbital deformations associated to the electric polarization via spin-orbit coupling can be probed through the quadrupole part of the scattering amplitude in a more general case[18] than the work of Hannon[15]. The diffraction patterns at the O K edge of Fig. 2a,c indeed provide information about the ordering of the orbital quadrupole moments reflecting the ferroelectric stripe networks. For the 71° domain walls, the diffraction peaks (‘1’ in Fig. 2a) correspond to a ferroelectric stripe pattern with a period of 218 nm ± 20 nm, as well as more intense ‘parasitic’ peaks (‘2’ in Fig. 2a at 49°) generated by the atomic steps stemming from the miscut of the substrate. This is fully consistent with atomic- and piezoforce- microscopy measurements (Methods and Supplementary Fig. 1). The case of the 109° sample is slightly subtler (Fig. 2c) as three populations can be identified. The intense round spots come from the atomic steps (‘1’ in Fig. 2c), while the two weaker ones (‘2’ & ‘3’ in Fig. 2c) come from the ferroelectric patterns. These correspond to two different period directions: the main (vertical) stripe structure and some less visible oblique terminations. Interestingly, these diffraction spots exhibit a clear circular dichroism (Fig. 2a,c), which disappears off-resonance (the full energy dependence is detailed in Supplementary Fig. 3). This dichroism happens for both systems and reaches 30 % for the main family of spots of the 109° DWs and 2% for the 71° DWs. The smaller dichroism of the latter is mainly due to the measuring angle, imposed by the blinding from the diffracted spots of the regular atomic steps at other angles.

Although X-rays cannot directly access electrical polarization in the electron-dipole approximation, they can however indirectly be sensitive to chiral polar arrangements[19,18]. The dichroism at the O K edge therefore indicates the presence of chirality in the ferroelectric order. This is only possible if the polarization does not vanish at the domain walls, which are non-Ising like, in agreement with recent reports[20]. This also imposes a homochiral FE winding (Fig. 2b,d), inconsistent with a zigzag winding of DWs linking in the simplest way, the polarizations on each side. It is easy to imagine how this is possible for 109° DWs as going from say the P_3^+ polarization direction of the first domain to the P_4^- of the second rotating via P_3^- or via P_4^+ are energetically degenerate (Fig. 2d). Thus, although we do not know what forces such a state, our measurements indicate that the two windings alternate: via P_3^- in one set of DWs and via P_4^+ for the neighbours, thus imposing a net chirality. Note that a slight dichroism is also visible at the Fe L edge (not shown), which finds a similar explanation as recently developed by Lovesey and van der Laan[18] and therefore corroborate the polar chirality in our systems. The case of the 71° DWs is more puzzling as a homochiral state imposes every second wall to wind in a ‘long angle’. For instance, when P directly rotates from P_4^- to P_3^- in one DW, it then goes

from P_3^- to P_3^+ then P_4^+ to reach P_4^- in the neighbouring one (Fig. 2b). This is obviously higher in energy than the direct P_3^- to P_4^- route and singles out the nature of this set of walls. Note here that P_3^+ and P_4^+ regions are not visible in the PFM images implying that they are narrow, but their presence makes the whole FE structure chiral.

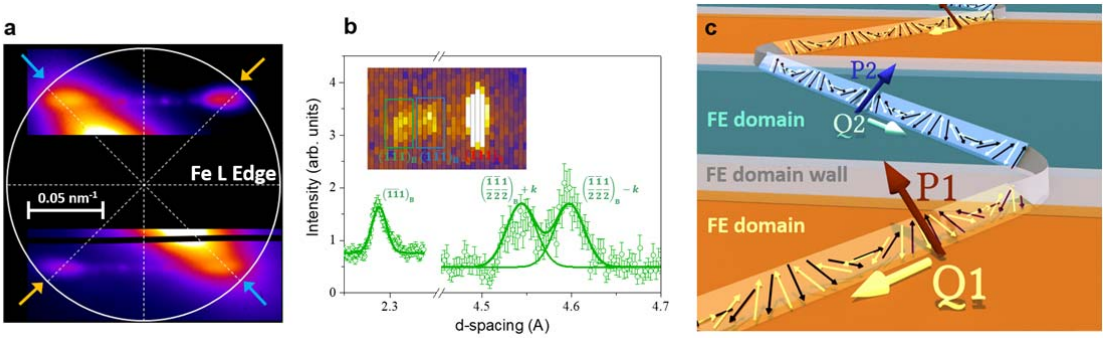

Figure 3: Non-collinear magnetic structure in ferroelectric domains by neutron and resonant X-ray scattering. **a**, X-ray diffraction at the Fe L edge (707.5 eV) for the 71° periodic ferroelectric patterns. The four main spots (pointed by blue and yellow arrows) visible in **a** stem from the two families of cycloids sketched in **c** and correspond to a cycloidal period of about 80 nm. **b**, Neutron scattering measurements (integrated intensity and 2D in inset) show the splitting of the Bragg peaks confirming the cycloidal order. Open circles are experimental data and solid lines are fits assuming a bulk-like spin cycloid with a period of 80 nm. **c**, Sketch of the two cycloids (one in each polarization domain) propagating in $BiFeO_3$. P_i and Q_i stand for the polarization vector of the domains and the wavevector of the cycloids, respectively.

Turning now to the magnetic order, the (circularly polarized) X-ray wavelength is tuned to the Fe L edge (Methods and Supplementary Fig. 2). The measured REXS diffraction patterns are now completely different, as four peaks appear in a square pattern as shown in Fig. 3a for the 71° FE stripe sample. These should be viewed as paired symmetrically with respect to the specular beam (thus in diagonal). They stem from two cycloidal families, one in each ferroelectric domain, with their propagation vector in the film plane and perpendicular to the local polarizations. This is also confirmed by time of flight neutron diffraction measurements (Fig. 3b, see Methods and Supplementary Fig. 5). Thus, only one out of the three symmetry allowed cycloidal families is present in each polarization domain (Fig. 3c), as the monoclinic distortion lowers further the initial 3-fold symmetry. The period is found to be 80 ± 8 nm, a little greater than the bulk period (64 nm). A closer examination of the elongated shape of the diffraction peaks indicates that they are actually composed of two spots, which stem from a splitting of the cycloidal AF peaks due to the modulation caused by the FE stripe pattern. Polarized X-rays and neutrons have the further capability to locate the spins direction, as previously demonstrated in BFO[21,22,23]. To our knowledge, the extra ability of both techniques to study the chiral nature of the AF arrangements has not been applied to BFO thin films. With their ultra-high intensity, synchrotron X-rays are the ideal probe of chirality in thin films. This was previously demonstrated in ferromagnets by analysing circular dichroism, i.e. the intensity difference between right and left polarized X-rays[24]. The magnetic scattering term used to measure ferromagnetic chirality is $-i\, f_1(\hat{\epsilon} \times \hat{\epsilon}') \cdot m_{\mathrm{n}}$. Here, we extend this type of analysis to antiferromagnetic chiralities through the $f_2(\hat{\epsilon}' \cdot m_{\mathrm{n}})(\hat{\epsilon} \cdot m_{\mathrm{n}})$ term, giving rise to diffraction peaks located at $2q_{\mathrm{cycloid}}$ in reciprocal space. Similarly, the dichroic plot of Fig. 4a for the 71° sample shows that $+q$ and $-q$ spots have opposite dichroism, indicating that the antiferromagnetic cycloids are chiral. This change of sign also reverses after an azimuthal sample rotation of 180° (Methods and Supplementary Fig. 4), which is consistent with a winding uniquely linked to the direction of P in each ferroelectric domain as expected theoretically[25] and measured in the bulk[23]. We point out here that this feature cannot be due to the (non-chiral) periodic magnetic uncompensation, which would appear at q_{cycloid} in reciprocal space.

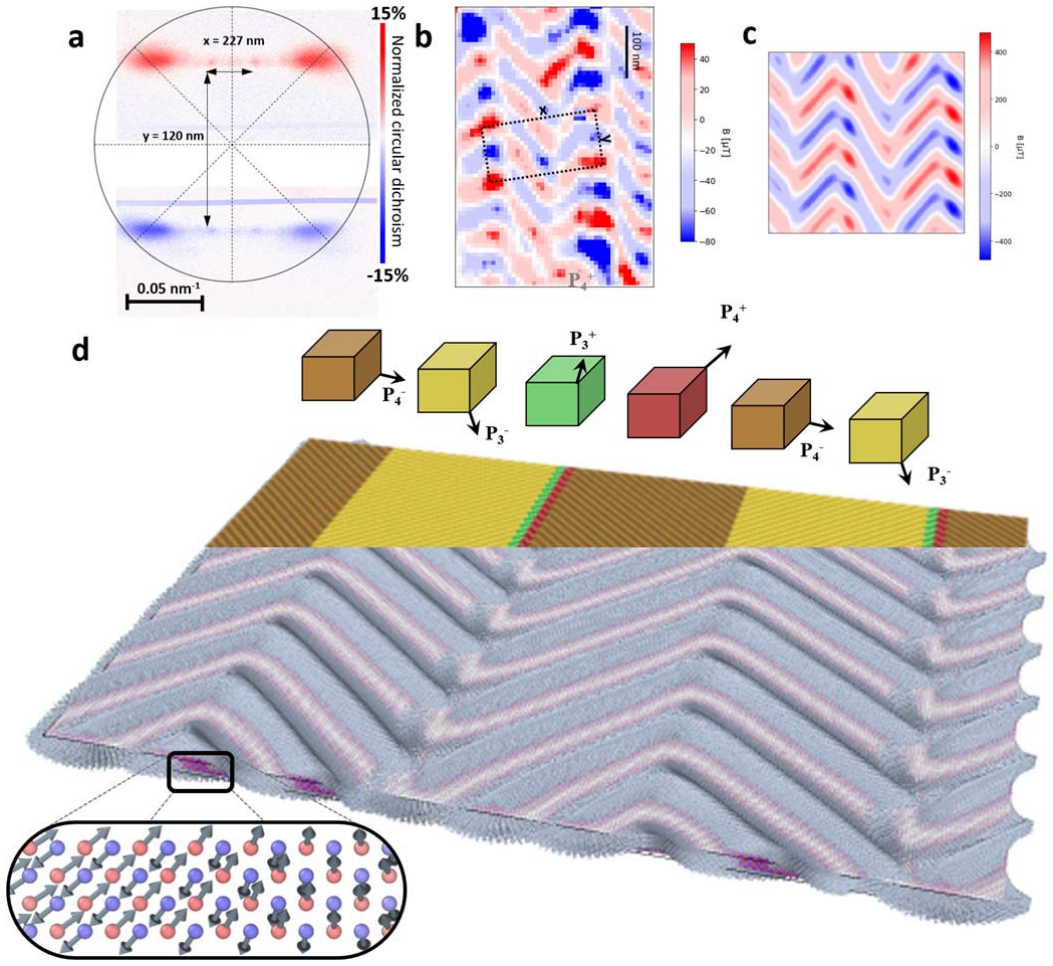

Figure 4: Chiral magnetic textures at ferroelectric domain walls seen in reciprocal and real spaces. a, Intensity difference between left and right X-ray polarizations for the two-cycloid system showing opposite dichroism for each set of diffraction spots taken as a signature of chirality. **b**, Scanning NV magnetometry image of the stray field 60 nm above the sample confirming in real space the two cycloidal populations and the rectangular array of bubbles at ferroelectric domain walls. **c**-**d**, Magnetic simulations using an atomistic code and showing the cycloidal arrangements in (a four-atom-thick slab of) the FE stripe domains, as well as their stitching at the walls (**d**). Every second wall, the polarization (black arrows) rotates along a long winding consistent with the chirality measured for the FE order. The stray field extracted from the simulations (**c**) shows excellent agreement with NV magnetometry in **b**.

In addition, the diffraction pattern of Fig. 4a comprises some extra features in the form of spots spreading along horizontal lines. These are representative of periodic structures generated by the FE stripes. Indeed, the two pairs of bright spots have a horizontal separation corresponding to the FE stripes' period of about 220 nm and a vertical separation giving 120 nm in real-space, close to the length of the cycloids projected onto the DWs ($\sqrt{2} \times 80$ nm). Therefore, this pattern results from the merging of the cycloids at the periodic domain walls. Importantly, its dichroic character indicates that the structures are chiral. Moreover, the weaker middle spots have an intensity inconsistent with the individual diffraction of two periodically striped cycloidal families. We thus attribute their presence to the diffraction of a chiral rectangular pattern stemming from the stitching of the cycloids.

To corroborate the presence of these chiral objects, we have combined REXS with real-space imaging by means of scanning NV magnetometry (Methods)[26,27]. Fig. 4b shows a magnetic image in a sample with 71° DWs grown under the exact same conditions. In addition to a vertical periodicity corresponding to the cycloids in different domains, regular bright spots are visible along one domain

wall out of two. They are therefore related to the different cycloidal windings. It is worth noting that in the simplest case of the short angle rotation of the ferroelectric polarization, the AF cycloid stitching can be straightforwardly almost continuous. In that case, the discontinuity in magnetization is minimum and the stray field should be close to that in the domain. On the other hand, for a wall with the FE polarization rotating along the long angle (as sketched in Fig. 2b), a frustration appears and the stitching is more complex. Interestingly, the measured hot spots on the scanning NV magnetometry image can be considered as the embryos of multi-q topological objects, especially as the dichroic diffraction patterns evidence their chirality. In order to better illustrate this DW effect, we have carried out numerical simulations using a dynamical atomistic magnetic simulations code[28]. We minimized the convergence time by dividing all distances by 10 and correspondingly multiplying by 10 the magnetoelectric interactions. This scaling does not affect the qualitative topography of the calculated magnetic configuration (Methods and Supplementary Fig. 6). The underlying striped FE state is taken with a 1-nm slab of a reversed polarization inserted every second wall to account for the 'reverse winding'. Fig. 4d shows the obtained spin arrangement where AF cycloids are clearly visible in the stripes and a peculiar stitching is observed on the walls where the FE polarization rotates along the wide angle. The stray field generated by the uncompensated moments shows excellent agreement with the recorded scanning NV magnetometry image (Fig. 4c) and notably the hot spots measured every second wall. This provides further evidence supporting our conclusions on both electric and magnetic chiralities. Because of the magnetoelectric interaction, these are entangled at domain walls to create very special entities. Our results call for a proper hybrid modelling of these peculiar objects and of their interplay with charge currents, spin currents and light, in analogy with the topological Hall effect[29] and related emergent electromagnetic phenomena[30] predicted for skyrmion systems.

Acknowledgments

We thank Horia Popescu for his assistance during the synchrotron runs, Antoine Barbier for discussions regarding diffraction as well as Yves Joly and Gerrit van der Laan for fruitful discussions about theoretical aspects of resonant x-ray scattering. We also acknowledge the company QNAMI for providing all-diamond scanning tips containing single NV defects. V.J. acknowledges financial support by the European Research Council (ERC-StG-2014, Imagine). The authors also acknowledge support from the French Agence Nationale de la Recherche (ANR) through projects Multidolls, PIAF and SANTA as well as the 'programme transversal CEA ACOSPIN and ELSA'. This work was also supported by a public grant overseen by the ANR as part of the 'Investissement d'Avenir' programme (LABEX NanoSaclay, ref. ANR-10-LABX-0035).

Authors contributions:

JYC, MV and NJ planned the REXS experiment and carried it out with CB. VG and SF prepared the samples and carried out the PFM measurements. BD, DK and PM carried out the neutron measurements while WA, IG, IF and VJ carried out the NV magnetometry. TC, JT and PT wrote, optimized and ran the simulation code. All authors participated in scientific discussions.

Data Availability: All relevant data are available from the authors, and/or are included with the manuscript.

References

1. Emori, S., Bauer, U., Ahn, S.-M., Martinez, E. & Beach, G. S. D. Current-driven dynamics of chiral ferromagnetic domain walls. *Nat. Mater.* **12**, 611–616 (2013).
2. Fert, A., Reyren, N. & Cros, V. Magnetic skyrmions: advances in physics and potential applications. *Nat. Rev. Mater.* **2**, 17031 (2017).
3. Barker, J. & Tretiakov, O. A. Static and Dynamical Properties of Antiferromagnetic Skyrmions in the Presence of Applied Current and Temperature. *Phys. Rev. Lett.* **116**, 147203 (2016).
4. Nahas, Y. *et al.* Discovery of stable skyrmionic state in ferroelectric nanocomposites. *Nat. Commun.* **6**, 8542 (2015).
5. Pereira Gonçalves, M. A., Escorihuela-Sayalero, C., Garca-Fernández, P., Junquera, J. & Íñiguez, J. Theoretical guidelines to create and tune electric skyrmion bubbles. *Sci. Adv.* **5**, eaau7023 (2019).
6. Jungwirth, T., Marti, X., Wadley, P. & Wunderlich, J. Antiferromagnetic spintronics. *Nat. Nanotechnol.* **11**, 231–241 (2016).
7. Wadley, P. *et al.* Electrical switching of an antiferromagnet. *Science* **351**, 587–590 (2016).
8. Smolenskii, G. A. & Chupis, I. E. Ferroelectromagnets. 20 (1982).
9. Dzyaloshinsky, I. A thermodynamic theory of "weak" ferromagnetism of antiferromagnetics. *J. Phys. Chem. Solids* **4**, 241–255 (1958).
10. Seidel, J. *et al.* Conduction at domain walls in oxide multiferroics. *Nat. Mater.* **8**, 229–234 (2009).
11. Van Aert, S. *et al.* Direct Observation of Ferrielectricity at Ferroelastic Domain Boundaries in $CaTiO_3$ by Electron Microscopy. *Adv. Mater.* **24**, 523–527 (2012).
12. Wei, X.-K. *et al.* Ferroelectric translational antiphase boundaries in nonpolar materials. *Nat. Commun.* **5**, (2014).

13. Bhattacharya, K. APPLIED PHYSICS: The Material Is the Machine. *Science* **307**, 53–54 (2005).
14. Catalan, G. & Scott, J. F. Physics and Applications of Bismuth Ferrite. *Adv. Mater.* **21**, 2463–2485 (2009).
15. Hannon, J. P., Trammell, G. T., Blume, M. & Gibbs, D. X-Ray Resonance Exchange Scattering. *Phys. Rev. Lett.* **61**, 1245–1248 (1988).
16. Hill, J. P. & McMorrow, D. F. X-ray Resonant Exchange Scattering: Polariztaion Dependence and Correlation Function. *Acta Crystallogr. A* **52**, 236–244 (1996).
17. van der Laan, G. Soft X-ray resonant magnetic scattering of magnetic nanostructures. *Comptes Rendus Phys.* **9**, 570–584 (2008).
18. Lovesey, S. W. & van der Laan, G. Resonant x-ray diffraction from chiral electric-polarization structures. *Phys. Rev. B* **98**, 155410 (2018).
19. Shafer, P. *et al.* Emergent chirality in the electric polarization texture of titanate superlattices. *Proc. Natl. Acad. Sci.* **115**, 915–920 (2018).
20. Cherifi-Hertel, S. *et al.* Non-Ising and chiral ferroelectric domain walls revealed by nonlinear optical microscopy. *Nat. Commun.* **8**, 15768 (2017).
21. Waterfield Price, N. *et al.* Coherent Magnetoelastic Domains in Multiferroic BiFeO 3 Films. *Phys. Rev. Lett.* **117**, (2016).
22. Lebeugle, D. *et al. Phys Rev Lett* **100**, 227602 (2008).
23. Johnson, R. D. *et al.* X-Ray Imaging and Multiferroic Coupling of Cycloidal Magnetic Domains in Ferroelectric Monodomain BiFeO 3. *Phys. Rev. Lett.* **110**, (2013).
24. Dürr, H. A. *et al.* Chiral magnetic domain structures in ultrathin FePd films. *Science* **284**, 2166–2168 (1999).
25. Mostovoy, M. Ferroelectricity in Spiral Magnets. *Phys. Rev. Lett.* **96**, (2006).

26. Rondin, L. *et al.* Magnetometry with nitrogen-vacancy defects in diamond. *Rep. Prog. Phys.* **77**, 056503 (2014).
27. Gross, I. *et al.* Real-space imaging of non-collinear antiferromagnetic order with a single-spin magnetometer. *Nature* **549**, 252–256 (2017).
28. Tranchida, J., Plimpton, S. J., Thibaudeau, P. & Thompson, A. P. Massively parallel symplectic algorithm for coupled magnetic spin dynamics and molecular dynamics. *J. Comput. Phys.* **372**, 406–425 (2018).
29. Bruno, P., Dugaev, V. K. & Taillefumier, M. Topological Hall Effect and Berry Phase in Magnetic Nanostructures. *Phys. Rev. Lett.* **93**, (2004).
30. Nagaosa, N. & Tokura, Y. Emergent electromagnetism in solids. *Phys. Scr.* **T146**, 014020 (2012).

Methods

Sample preparation and characterization

The epitaxial thin film heterostructures were grown by pulsed laser deposition using a KrF excimer laser (λ = 248 nm, 1 J cm−2) on an orthorhombic $DyScO_3$ (110)o single crystal substrate. The $SrRuO_3$ (resp. $La_{1/3}S_{2/3}rMnO_3$) bottom electrode (1.2 nm) was grown with 5 Hz repetition rate at 650 °C under 0.2 mbar of oxygen for the sample exhibiting 71° (resp. 109°) stripe domains. The $BiFeO_3$ films (32 nm) were subsequently grown at 650 °C under 0.36 mbar of oxygen at 1 Hz repetition rate. The heterostructures were slowly cooled down under high oxygen pressure. In both cases, the film surface exhibits single-unit-cell atomic steps (with additional ferroelastic deformations related to the ferroelectric variants of the 109° sample).

The structural thin film properties were assessed by X-ray diffraction (XRD, Xpert Panalytical) performing reciprocal space mappings (RSMs) along different directions of the monoclinic $DyScO_3$ substrate. PFM experiments were conducted with an atomic force microscope (Nanoscope V multimode, Bruker) and two external SR830 lock-in detectors (Stanford Research) for simultaneous acquisition of in-plane and out-of-plane responses. A DS360 external source (Stanford Research) was used to apply the AC excitation to the bottom electrodes at a frequency of 35 kHz while the conducting Pt coated tip was grounded. The ferroelectric configurations of the pristine BFO samples were identified by vectorial PFM, i.e. probing the different in-plane variants when rotating the sample crystallographic axes compared to the PFM cantilever long axis. Alternated light/dark stripes are observed in the in-plane PFM phase image acquired with the cantilever aligned along the pseudo-cubic $[100]_C$ direction.

The PFM and AFM images show structures that can be compared to the resonant scattering diffraction through FFT transforms. Two different features can be attributed to diffraction by substrate atomic steps and electrical polarization stripes, but peak No3 of the REXS does not appear in the PFM+AFM images. We attribute it to some domains' terminations, which can be guessed from the real-space PFM image but not ordered enough to appear in the Fourier transforms.

Resonant soft x-ray elastic scattering

A. Experimental details and setup configuration

The experiment has been performed at SOLEIL synchrotron on the SEXTANTS beamline in the RESOXS [31] diffractometer. The diffractometer is equipped with a CCD camera (2048x2048 pixels of 13.5µm) that is on the detector arm at 26 cm from the sample. The solid angle probed by the camera alone is 6.3° but it can be further moved perpendicularly to the scattering plane by +/- 15mm to increase the accessible reciprocal space. A set of beamstops placed a few mm before the CCD chip can be precisely aligned with few 10nm precision in order to block the specular beam or unwanted strong Bragg reflections.

Data were collected at both O K edge and Fe L edges using circularly polarized x-rays delivered from an Apple 2 undulator located at the I14M straight section of SOLEIL storage ring. A typical photon flux of 10^{13}ph/s with 100meV energy resolution was used for the experiment.

B. Energy dependence

Prior to any conclusions relating to circular dichroism and chirality, the energy dependence of circular dichroic diffraction patterns has been measured both around the Fe L_3 edge and the O K edge. Supplementary Fig. 2 presents the normalized circular dichroism for the upper diffraction pattern as

function of the incident photon energy around the Fe L_3 edge. The dashed line stands for the normalized specular intensity at an incident x-ray angle of 30°. On the left side of the figure, a selection of normalized circular dichroisms of the cycloidal diffraction patterns are presented. As expected, there is no signal off-resonance and two maxima are observed for the 2p to 3d t_{2g} transition (707.5 eV) and about 1 eV above the 2p to 3d e_g transition (710 eV). However, when reaching the maximum of the main resonance (709 eV), the circular dichroism is either vanishing or even reversing. Yet, at this energy, the intensity is one order of magnitude larger and additional effects might play a non-negligible role. Indeed, dynamical effects and phenomena such as x-ray birefringence [32] or magneto-optical effects [33] are known to occur. One crucial consequence is that the X-ray polarization could be modified during the crossing of the material (and not only by scattering processes). Because it is challenging to account for these processes, we have avoided this energy for the analysis of the magnetic chirality. A similar argument holds for the O K edge, as can be seen in Supplementary Fig. 3. A strong energy dependence is evidenced, yet no inversion of circular dichroism is observed in the peaks under consideration. It is interesting to notice that the maxima in circular dichroism are found in the feet of the main resonances.

C. Azimuthal dependence

Topological structures generate a dichroic signal that is of opposite sign in +q and –q. This depends on the sign of the chirality and it is therefore linked to the antiferromagnetic winding in the sample. This provides us with another means to further confirm that the dichroism stems from the AF cycloids. Indeed, as Supplementary Fig. 4 shows, the dichroism reverses when the sample is rotated by 180° in the azimuthal plane.

Neutron scattering

We used time of flight neutron diffraction to confirm the presence of the cycloidal ordering in our BFO/DSO thin film. The measurements were carried out in four different scattering geometries schematically shown in Supplementary Fig. 5. For each sample orientation (angle ϕ in Supplementary Fig. 5a), two distinct pseudo-cubic diagonals $\{111\}_D$-type, referring to the DSO substrate unit cell, were in the scattering plane, but as only one of them could be optimized with respect to the neutron flux and resolution for the target magnetic reflections, two measurements (angle ω in Supplementary Fig. 5a) were performed. The target reflections were the satellites of the {½½½}±k type expected at a *d*-spacing range around 4.5-4.6 Å. The measurements were performed at high scattering angles (typically above 120°) to achieve a good momentum transfer resolution and the reflecting geometry helped to avoid absorption from the substrate. After 16 hours of exposition time, the (hhh)-type reflections of the BFO film could be clearly observed (Supplementary Fig. 5b,c). In two out of the four scattering geometries, two signals, spatially separated from the substrate on the detectors array, could be resolved (Supplementary Fig. 5b), revealing the presence of structural domains. In the other two measurements, the domains could not be resolved (Supplementary Fig. 5c). Data, focused around these (hhh)-type reflections and plotted as a function of d-spacing, are presented in Supplementary Fig. 5d-f. The patterns clearly reveal the presence of magnetic reflections in the expected d-spacing range. The magnetic satellites scatter very close to the nuclear (hhh)-type reflections and the angular resolution of the data is not sufficient to spatially isolate the nuclear and magnetic reflections on the detector array. The d-spacing positions and intensities of the observed magnetic reflections can be quantitatively fitted by the model implying a cycloidal magnetic order, similar to that in bulk BFO, and the presence of two equi-populated ferroelectric domains illustrated in Supplementary Fig. 5g,h. It is remarkable that the data can be satisfactorily modelled only assuming a single magnetic domain state with the propagation vector k=(-δ,0,δ), δ≈0.043(3) for both ferroelectric domains. As possible reasons for suppression of the other two magnetic domains

with $k_2=(0,-\delta,\delta)$ and $k_3=(-\delta,\delta,0)$ is the small monoclinic distortion of the ferroelectric domains imposed by the misfit with the substrate as discussed below.

The pseudocubic unit cell metric of the orthorhombic DSO substrate (Supplementary Fig. 5i) is characterised by two distances ($a_D=c_D\neq b_D$) and one angle ($\beta_D\neq 90$). This implies two non-equivalent {100}-type BFO films with the b_D-axis either parallel or perpendicular to the surface. In our case, the b_D-axis is parallel to the surface. The unit cell is also characterised by two long $[11\text{-}1]_D/[1\text{-}1\text{-}1]_D$ and two short $[111]_D/[1\text{-}11]_D$ diagonals as shown in Supplementary Fig. 5i. Our neutron diffraction data indicate that this type of substrate imposes a selection of two ferroelectric domains in the BFO film. The polar [111] axes of these domains are along the long diagonals $[11\text{-}1]_D$ and $[1\text{-}1\text{-}1]_D$ of the substrate (Supplementary Fig. 5g-i). Moreover, the pseudocubic unit cell metric of the BFO film ($a_f=b_f=c_f$, $\alpha_f=\beta_f=\gamma_f\neq 90°$) does not match the metric of the substrate, resulting in additional structural distortions. These could be responsible for the selection of the single magnetic domain state, through magneto-elastic coupling, within the structural ferroelectric domains. The resolution of our neutron diffraction data, however, is not sufficient to directly measure these distortions.

In the scattering geometries optimized to measure magnetic satellites, close to the $(11\text{-}1)_D$ and $(1\text{-}1\text{-}1)_D$ reflections, the two domains cannot be separated and a contribution from both domains is present in the focused data (Supplementary Fig. 5c,f). The refined value of the propagation vector $\delta=0.043(3)$ is slightly smaller than that of the bulk BFO indicating a slightly longer period of the cycloidal modulation with respect to that of the bulk. This is in a good agreement with the synchrotron data.

Scanning NV magnetometry

Scanning-NV magnetometry is performed with a commercial all-diamond scanning-probe tip containing a single NV defect (QNAMI, Quantilever MX). This tip is integrated into a tuning-fork-based atomic force microscope (AFM) combined with a confocal microscope optimized for single defect spectroscopy. Details about the experimental setup can be found in [34]. Quantitative magnetic field distributions are obtained by monitoring the Zeeman shift of the NV defect electron spin sublevels through optical detection of the magnetic resonance [35]. Experiments are performed under ambient conditions with a NV-to-sample distance of 60 nm.

Atomistic spin dynamic computation

Unlike micromagnetic simulations applied to ferromagnets, large-scale simulations of complex antiferromagnetic textures remain a challenge. Indeed, the micromagnetic approximation consisting in averaging local magnetic moments into large enough computational cells and supposing that this quantity only changes in direction and not in magnitude, fails for antiferromagnets. In order to provide a simulation support for our experimental findings, atomistic spin dynamics simulations have been performed where each atom carries a spin. The relevant interactions for BFO have been considered, namely exchange, magnetoelectric, anisotropy and asymmetric Dzyaloshinskii-Moriya interactions on a periodically striped ferroelectric pattern. In order to model as closely as possible the antiferromagnetic configurations of our samples, the ferroelectric domain walls have been designed as measured, with a chiral winding. For the 71° pattern, one wall out of two was taken to rotate following the 'long winding' schematically represented in Fig. 4b of the main text. The simulations have been carried out using the SPIN package of LAMMPS [36, 37] which assesses spin textures and their dynamics by solving the Landau-Lifshitz-Gilbert (LLG) equation :

$$\frac{ds_i}{dt} = \omega_i \times s_i + \alpha s_i \times \frac{ds_i}{dt}$$

with s_i the unit spin vector at the i[th] position, α the Gilbert damping coefficient and ω_i the effective spin pulsation defined as:

$$\omega_i = \frac{-1}{\hbar}\frac{\partial H}{\partial s_i}$$

For the present study, the three main components of the Hamiltonian (H) of N interacting spins are considered, namely the symmetric exchange, the magneto-electric (ME) and the asymmetric Dzyaloshiskii-Moriya interactions (DM) expressed as follows:

$$H = -\sum_{i,j,i\neq j}^{N} J_{ij}\, s_i \cdot s_j + \left(P \times e_{ij}\right) \cdot \left(s_i \times s_j\right) + \left(p \times e_{ij}\right) \cdot \left(s_i \times s_j\right)$$

with J_{ij} the symmetric exchange coefficient, e_{ij} the unit direction vector between the i[th] and j[th] spins, P the global ferroelectric polarization and p the local polarization induced by the octahedral tilts and alternating from site to site. Noteworthy, the consequence of this latter is the small cycloidal wriggling leading to an apparent spin density wave.

The simulations have been performed for N=N_x (240)*N_y (172)*N_z(4) spins with periodic boundary conditions in x and z. A cubic lattice with a 3.96 Å constant was considered. The x-direction corresponds to the (100) crystallographic direction. Note that while the antiferromagnetic exchange interaction has been kept to its known value (-4.5 meV for nearest neighbour interaction), ME and DM interactions were multiplied by a factor 10 (1.09 meV and 0.54 meV respectively) to reduce the simulated volume and hence the calculation time. The cycloidal period scales correspondingly.

The spins are divided into 60 atom wide stripes with different orientations of P in order to mimic the 71° ferroelectric striped pattern. Every second ferroelectric domain wall is defined following the assumptions explained in the article. The result is shown in Supplementary Fig. 6.

Subsequently, the magnetic stray field of the converged spin texture is calculated and projected along the NV defect quantization axis [34], leading to the result shown in figure 4 d of the main article.

References

[31] N. Jaouen, J.-M. Tonnerre, G. Kapoujian, P. Taunier, J.-P. Roux, D. Raoux, and F. Sirotti, J. Synchrotron Radiat. 11, 353 (2004).

[32] Y. Joly, S. P. Collins, S. Grenier, H. C. N. Tolentino, and M. De Santis, Phys. Rev. B 86, 220101 (2012).

[33] M. W. Haverkort, N. Hollmann, I. P. Krug, and A. Tanaka, Phys. Rev. B 82, 094403 (2010).

[34] L. Rondin et al., Appl. Phys. Lett. **100**, 153118 (2012).

[35] L. Rondin, et al., Rep. Prog. Phys. **77**, 056503 (2014).

[36] S. Plimpton, J. Comput. Phys. 117, 1 (1995).

[37] J. Tranchida, S. J. Plimpton, P. Thibaudeau, and A. P. Thompson, J. Comput. Phys. 372, 406 (2018).

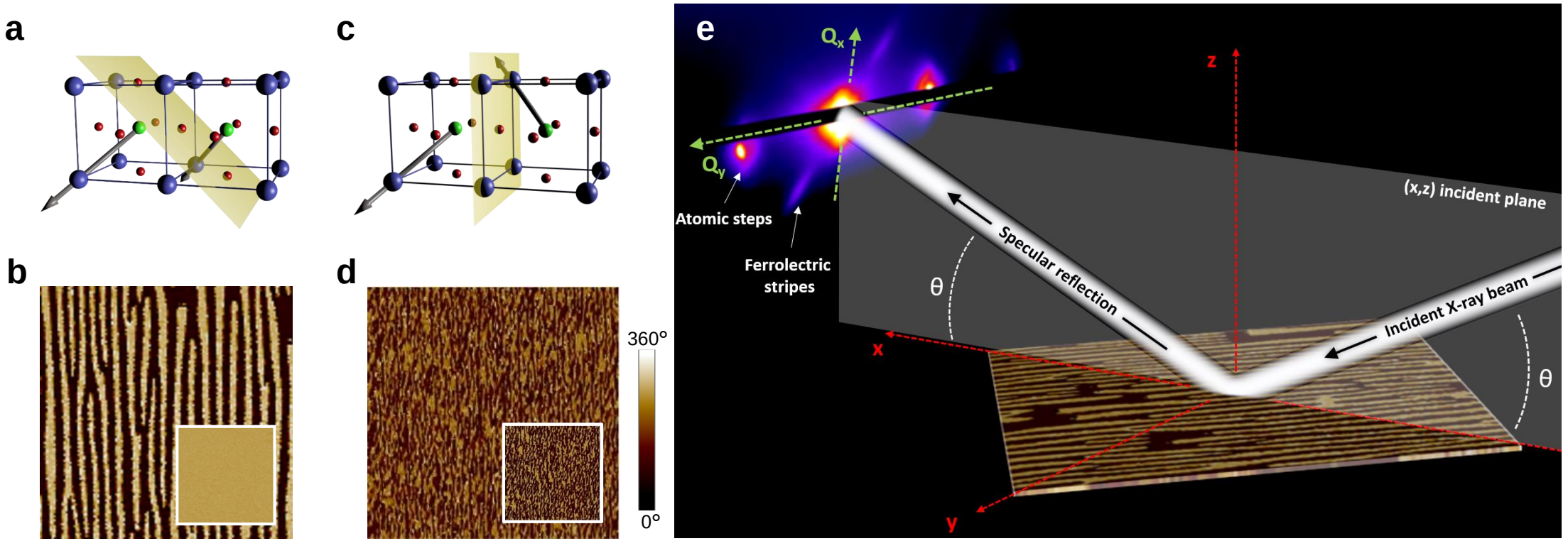
a
c
b
d
360°
0°
e
Q_x
Q_y
z
(x,z) incident plane
Atomic steps
Ferrolectric
stripes
Specular reflection
Incident X-ray beam
θ
θ
x
y

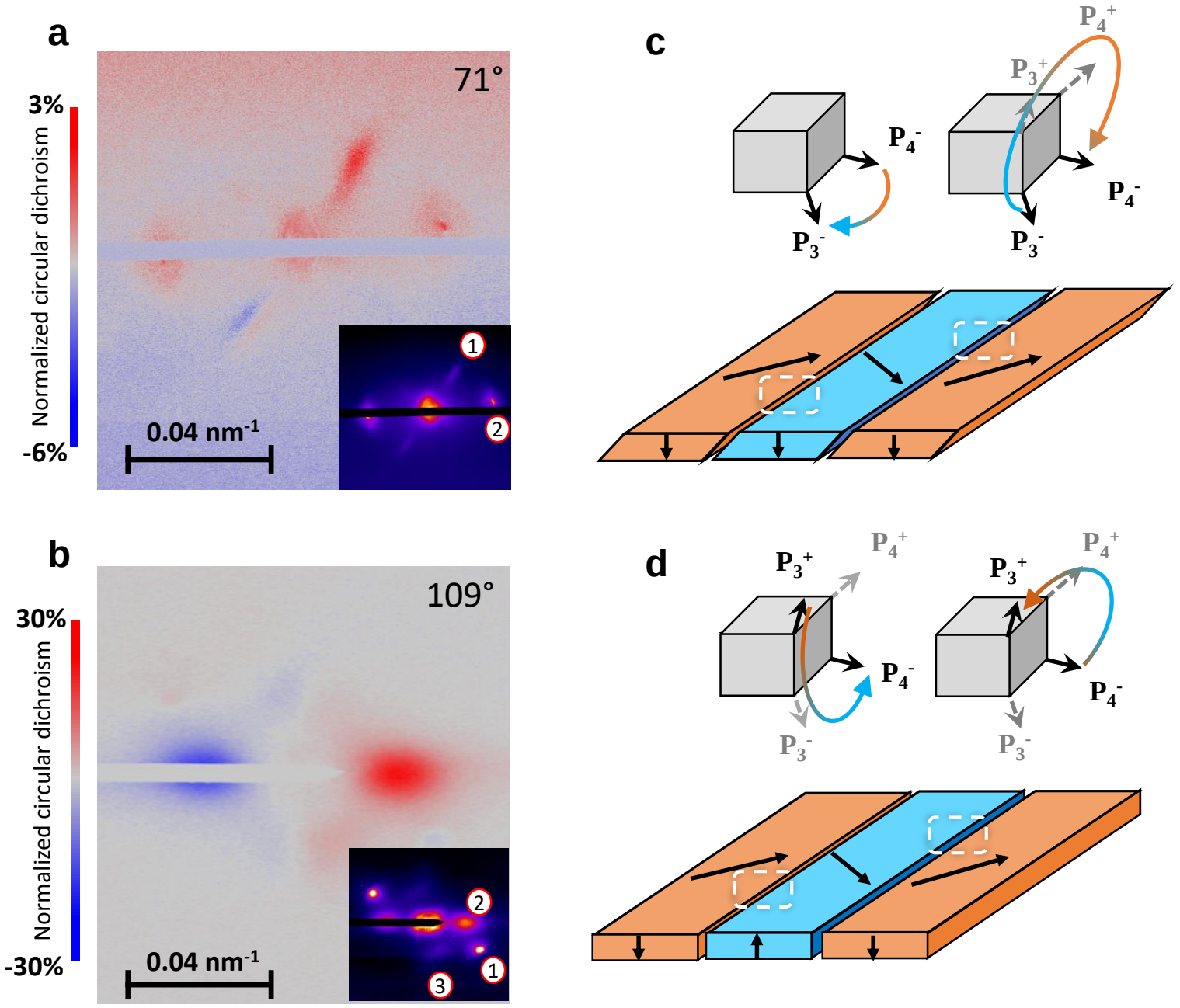
a
71°
3%
Normalized circular dichroism
-6%
0.04 nm-1
1
2
b
109°
30%
Normalized circular dichroism
-30%
0.04 nm-1
1
2
3
c
P4+
P3+
P4-
P3-
P4-
P3-
d
P3+
P4+
P4-
P3-
P3+
P4+
P4-
P3-

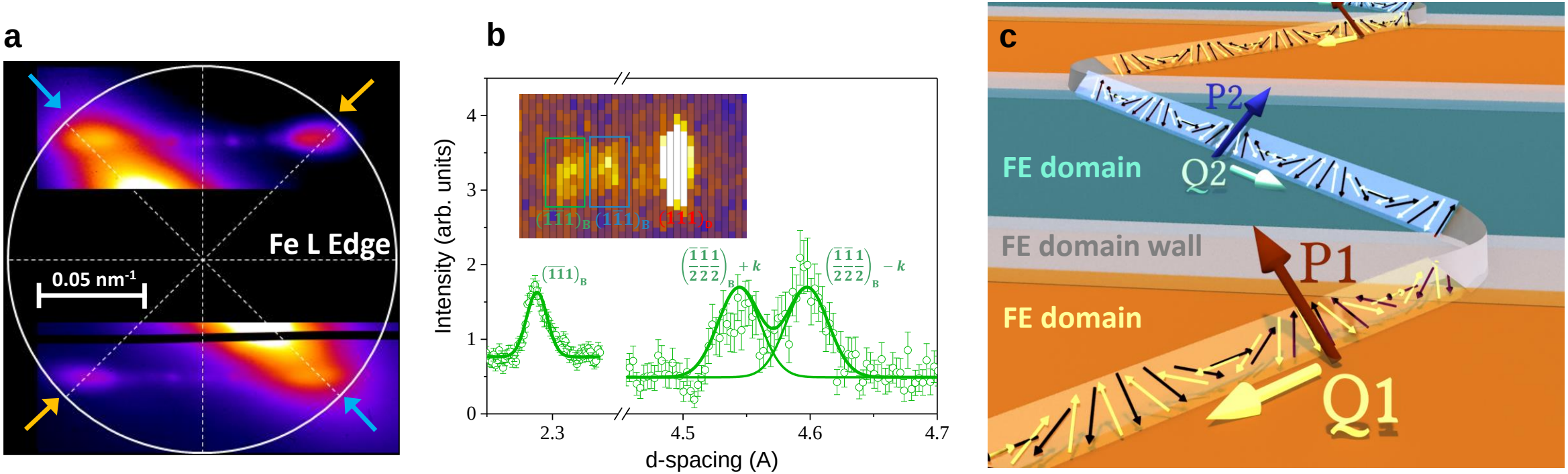
a
Fe L Edge
0.05 nm-1
b
Intensity (arb. units)
d-spacing (A)
2.3
4.5
4.6
4.7
c
P2
Q2
FE domain
FE domain wall
P1
FE domain
Q1

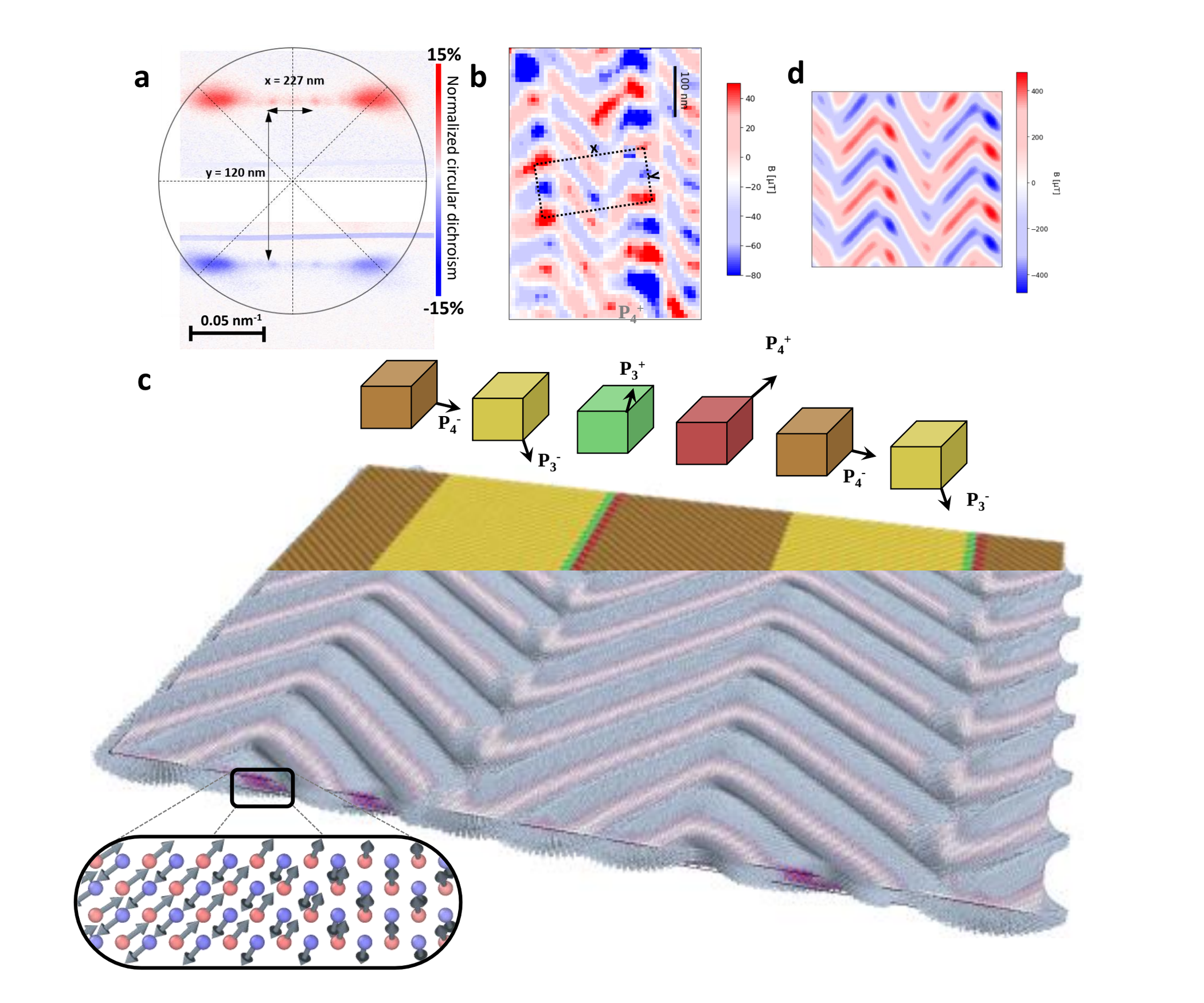
a
x = 227 nm
y = 120 nm
0.05 nm-1
15%
Normalized circular dichroism
-15%
b
100 nm
x
y
P4+
40
20
0
−20
−40
−60
−80
B [μT]
d
400
200
0
−200
−400
B [μT]
c
P4-
P3-
P3+
P4+
P4-
P3-